S1 Illustration of a U_{RS} event

Figure S1 shows the May 8, 2019 POI 8-3 event of what appears, in the lidar profile and in terms of relatively strong $R_{log}(\tau_c \; vs \; \tau_U^{\ell})$ correlation (0.83), to be a relatively weak τ_{dust}^{ℓ} dust event. However, $R_{log}\left(\tau_{dust}^{\ell} \; vs \; v_{dust}(0)\right)$ was relatively small (0.42) so that the event did not achieve the "*D*" classification) while the strong $R_{log}(\tau_c \; vs \; \tau_U^{\ell})$ correlation resulted in the U_{RS} subclass. That large value and, more specifically, the appearance of the plume as well as the rather striking τ_c vs τ_U^{ℓ} temporal correlation seen in Fig. S1, suggests that (i) this POI is likely a dust event that is detectable at the columnar scale while (ii) the low $R_{log}\left(\tau_{dust}^{\ell} \; vs \; v_{dust}(0)\right)$ might be ascribed to local $v_{dust}(0)$ variations that do not register[1] in (have no apparent influence on) co-related variations of τ_c and τ_D^{ℓ}.

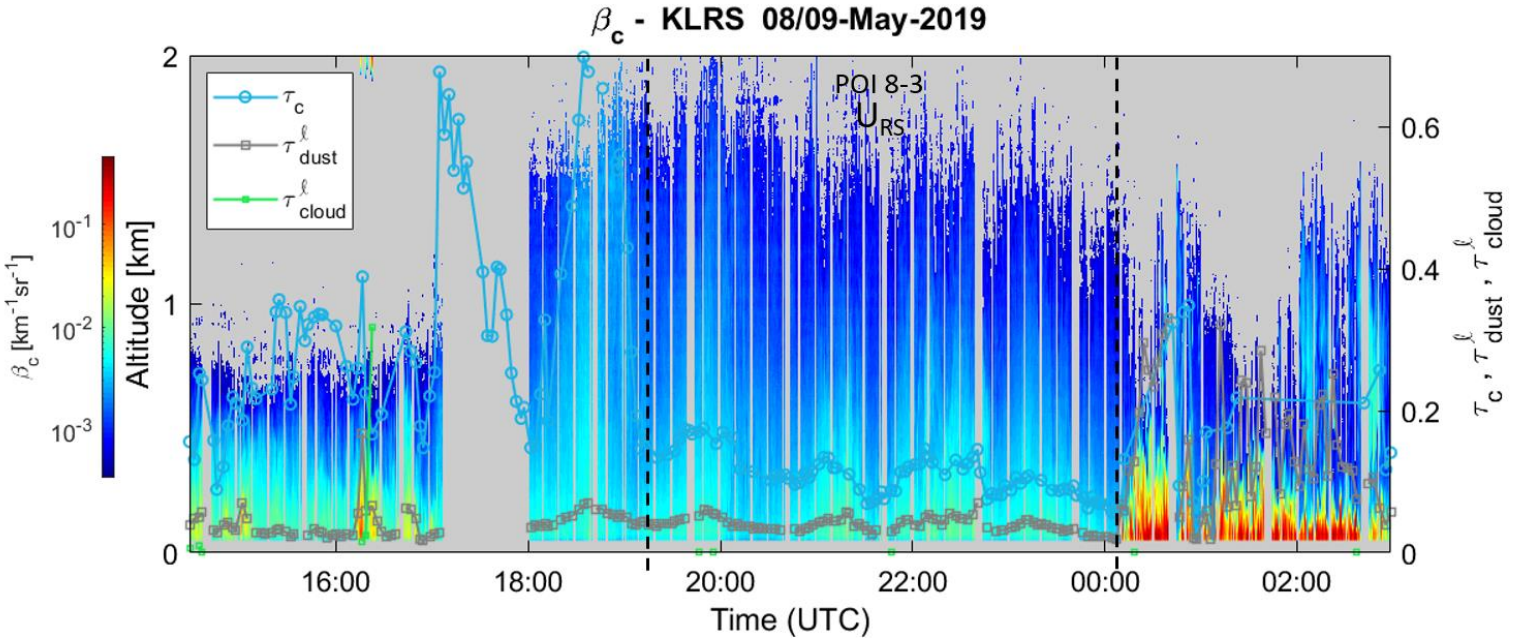

Figure S1: May 8, 2019 illustration of what appears to be a dust event (between 19:00 and 24:00 UTC) with clear $(\tau_c \; vs \; \tau_D^{\ell})$ correlation. At the same time the $\tau_{dust}^{\ell} \; vs \; v_{dust}(0)$ correlation was relatively weak (see more contextual details in Sect. S6).

[1] or only weakly register if we keep in mind the artificial nature of a hardcoded threshold of $R_{log}\left(\tau_{dust}^{\ell} \; vs \; v_{dust}(0)\right) = 0.5$)

S2 Illustration of the dust layer height estimation process

Figure S2 illustrates a day (May 7) that included a D event between the two red-colored, dashed vertical lines. The τ^{ℓ}_{dust} vs $v_{dust}(0)$ correlation coefficient (R) was significant (0.79) and the plume-like nature of the $\beta_{c,\sim}$ profile support the affirmation of robust dust plume.

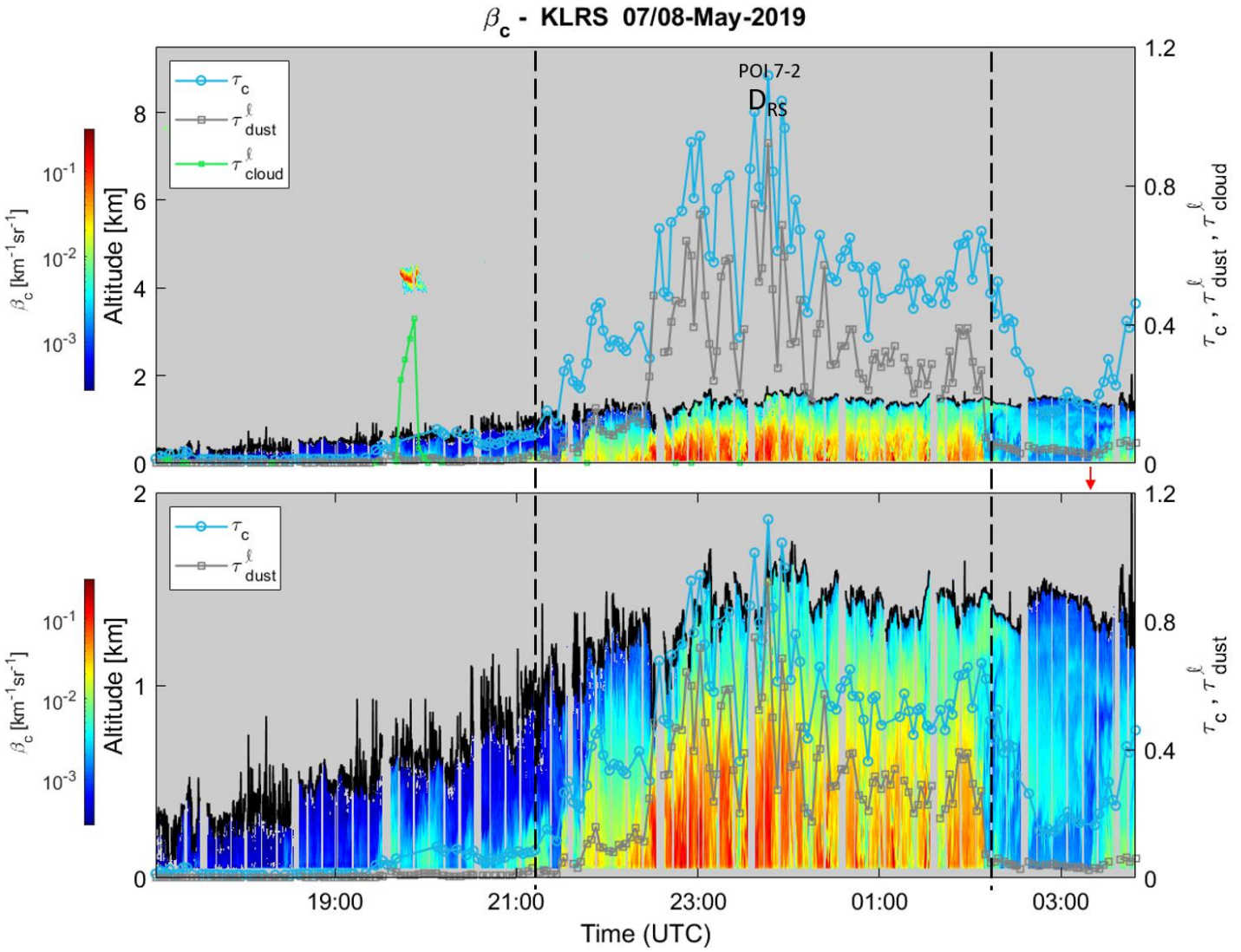

Figure S2: Illustration (between the red dashed vertical lines) of what appears to be a strong D_{RS} event on May 7, 2021.

The black-colored part of Fig. S2 shows the result of the automated dust layer height (DLH) process that was applied to the $\beta_{c,\sim}$ profiles (it often appears to be somewhat higher than the apparent top of the $\beta_{c,\sim}$ profiles because the DLH routines seeks out any non-zero $\beta_{c,\sim}$ values and a sparse scattering of such values often appears above the more contiguous portion of the profile). The process verifies that the upper level (UL) of each contiguous segment[2] in each $\beta_{c,\sim}$ column is lower than the user specified MCA (minimum cloud altitude). If the condition is satisfied, then the UL of the highest segment is considered as the DLH for that column. The algorithm (in those columns for which at least one UL is higher than the MCA) computes the P($max(mean(\beta_{c,\sim})$) value of all the sub-MCA contiguous segments in segment number i_P: if $\mathrm{UL}_{i_P} < MCA$, for all i_P values then the UL of the highest contiguous segment is considered as the DLH. Otherwise, if a lower part of segment i_P is lower than the MCA then the UL of that lower part is labelled the DLH.

S3 Illustration of the correlation analysis and optimal bin resolution

In this section we illustrate the coherency between τ_{dust}^{ℓ} and $v_{dust}(0)$ measurements using linear and logarithmic scale analysis for a known dust event. A high correlation between those two independent parameters is, we believe, a strong argument for having identified a local dust plume that has a good potential of being remotely sensed. In some cases, the linear scattergram is excessively influenced by a few points (what amounts to a poorly sampled distribution). For instance, the log-log scattergram of Fig. S3b, appears to indicate a multi-scale correlation (compared with a near-zero mass of points in the linear scattergram whose *R* value would tend to be dominated by points far from the origin). Figure S3a shows the actual linear and log temporal profiles for two bin resolutions (1 minute and 24 minutes written 1^{m} and 24^{m}).

The noise evident in the 1^{m} curves of Fig. S3a suggests that some measure of time-bin averaging might improve correlation statistics. An analysis of $R\left(\tau_{dust}^{\ell}\ vs\ v_{dust}(0)\right)$ and $R_{log}\left(\tau_{dust}^{\ell}\ vs\ v_{dust}(0)\right)$ vs time-bin resolution was accordingly performed in order to analyze the influence of bin resolution and the importance of seeking an optical bin resolution. Figure S3c illustrates the results for the dust event of May 7. A minimum of N = 10 samples was considered as a threshold of points for acceptable correlation statistics. The Fig. S3c illustration underscores a general affirmation: that *R* values were not strongly dependent on bin resolution (they were, not surprisingly, strongly dependent when the number of bins was < 10).

[2] contiguous segments are contiguous (non-zero) $\beta_{c,\sim}$ segments between NAN pixels or NAN segments. These can include single pixel segments that are often found above the more contiguous part of the profiles

τ^{ℓ}_{dust} and $\nu_{dust}(0)$ time series - KLRS 07/08-May-2019

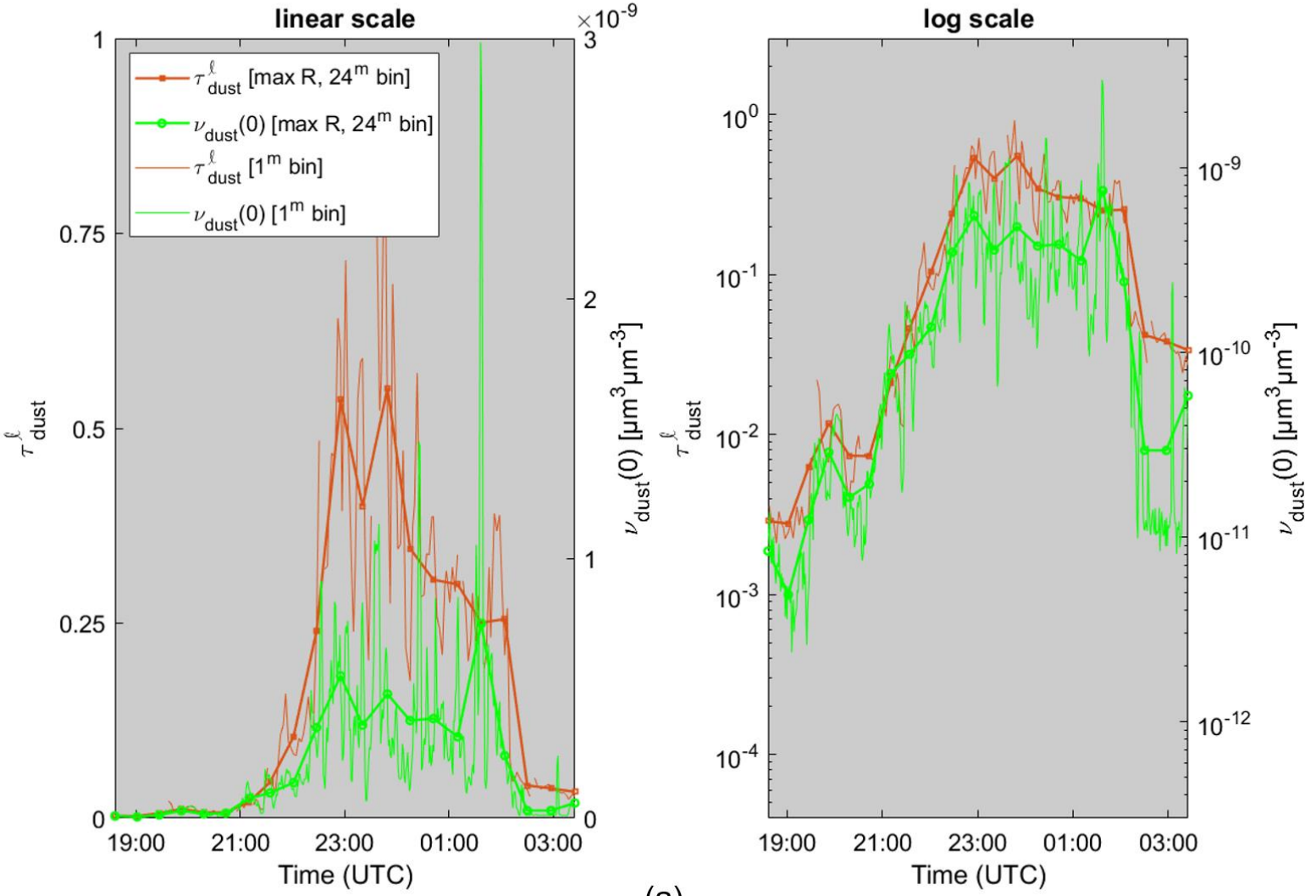

(a)

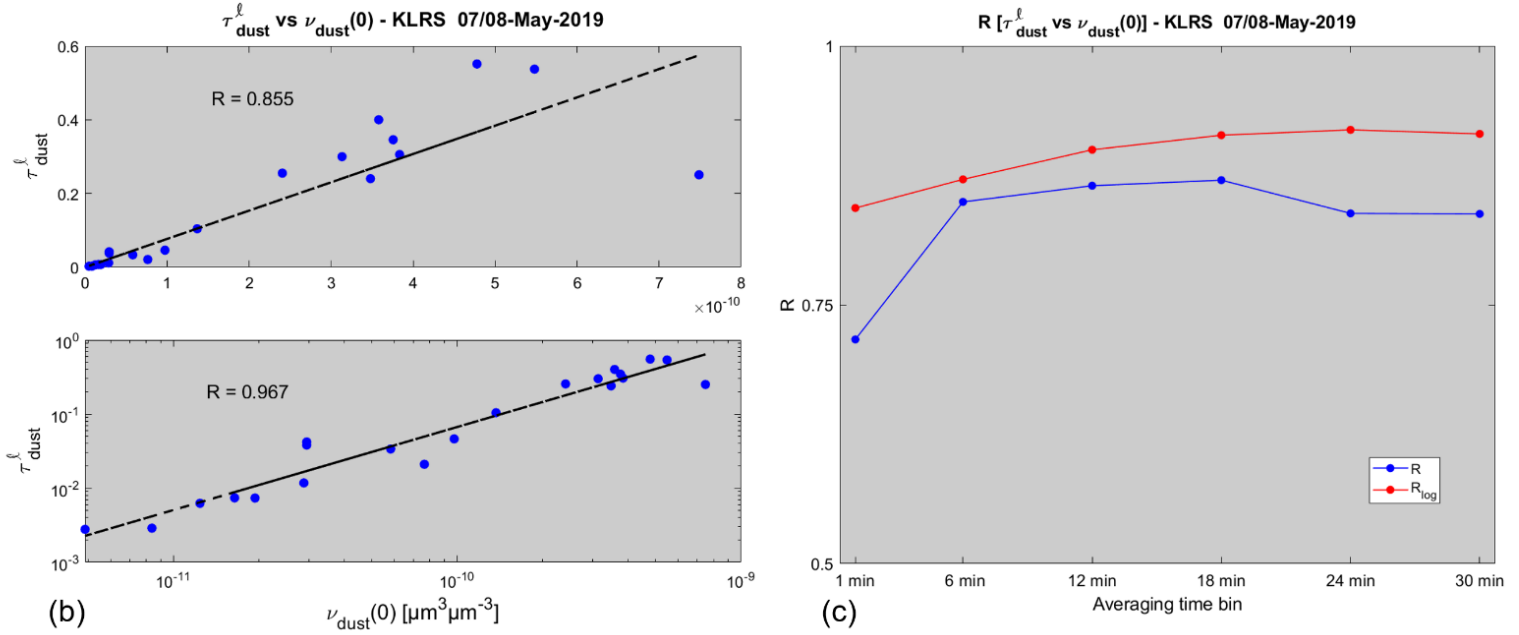

Figure S3: (a) May 7 time series of τ_{dust}^{ℓ} and $v_{dust}(0)$ (linear and logarithmic spaces) for the finest bin resolution of 1 minute and for an optimal bin resolution of 24 minutes. (b) τ_{dust}^{ℓ} vs $v_{dust}(0)$ scattergrams in linear (top) and logarithmic (bottom) space for the optimal bin resolution of 24 minutes (corresponding to the thicker slowly varying curves of Fig. S3a). (c) $R\left(\tau_{dust}^{\ell}\ vs\ v_{dust}(0)\right)$ optimal bin analysis for May 7, 2019.

S4 Supplements of Fig. 6

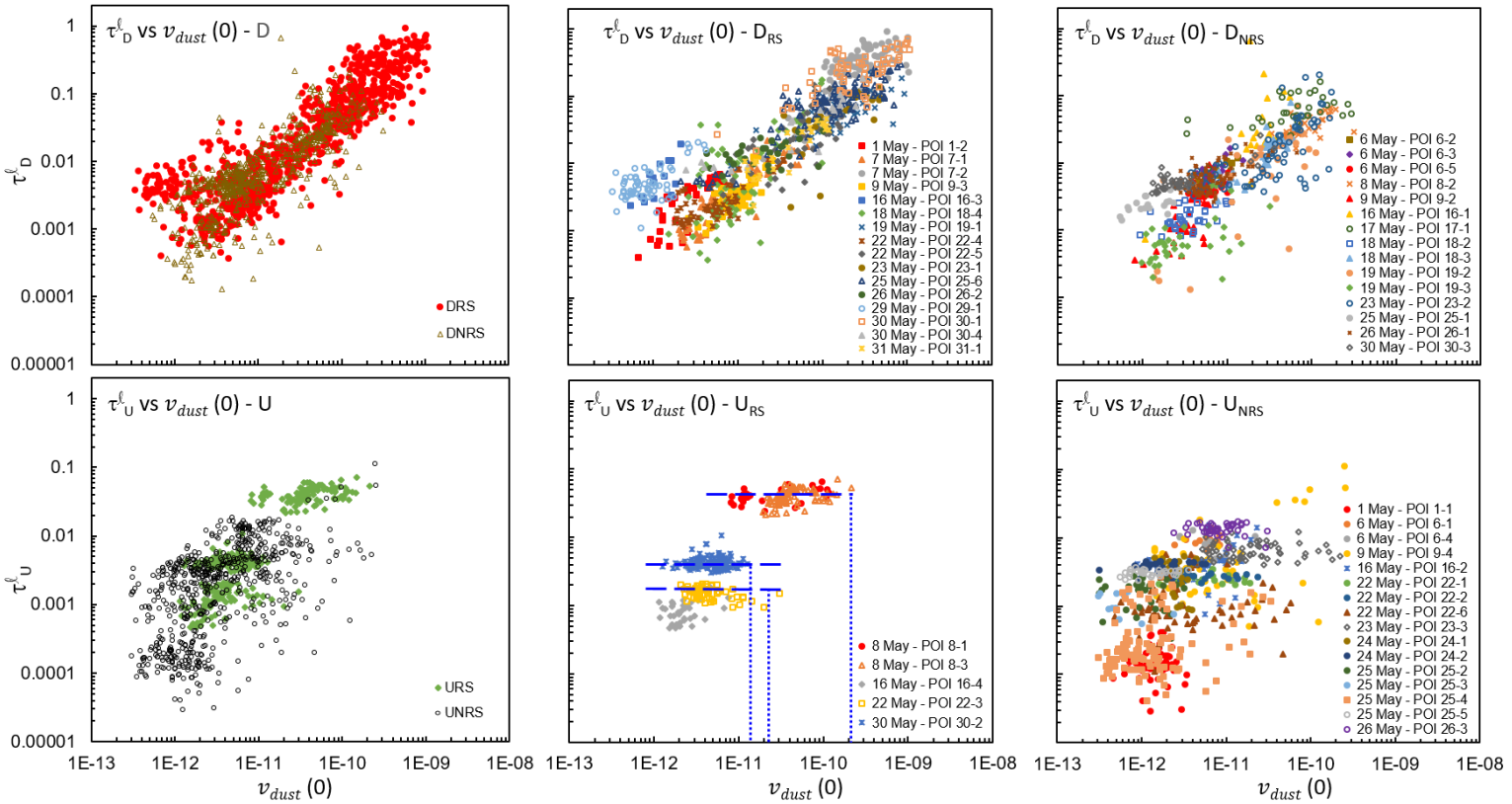

Figure S4: Subclass details of Fig. 6. The multiple blue dashed-lines on the U_{RS} plot represent the τ^{ℓ}_{dust} "bottoming out" effect while the vertical dotted lines represents the $v_{dust}(0)$ thresholds as a function of different specific events.

S5 Weighted and unweighted regression averages of S_c

Figure S5 shows the variation of POI-dependent $\langle S_c \rangle_{\omega}$ values (units of sr) as a function of the weights employed in computing $\langle S_c \rangle_{\omega}$. As expected, the unweighted variants ($\langle S_c \rangle$) appear to be more variable. The $\langle S_c \rangle_{\omega}$ values tend to bottom out at large $\langle \omega \rangle$ values (weighted average of $28.0 \pm 3.3\ sr$).

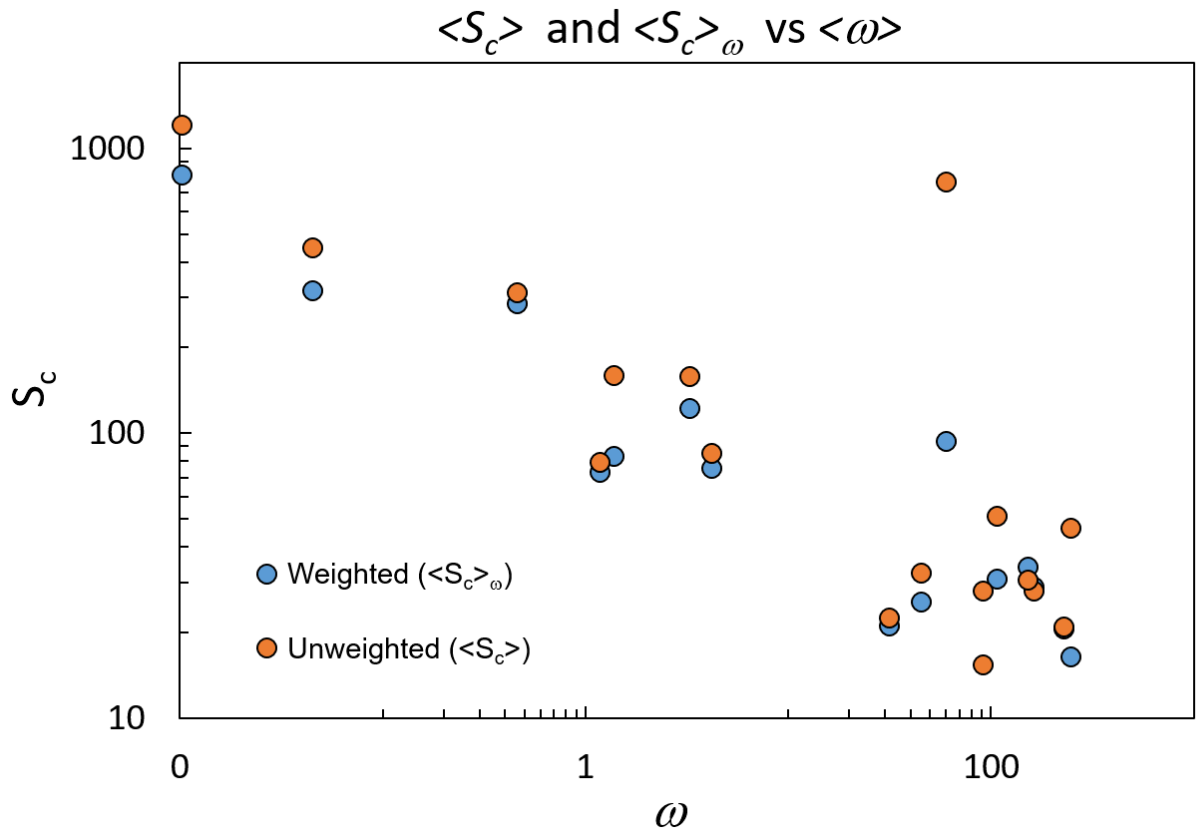

Figure S5: Regression-derived weighted and unweighted averages ($\langle S_c \rangle_\omega$ and $\langle S_c \rangle$) as a function of the weights (ω) employed to compute $\langle S_c \rangle_\omega$ (see Appendix A1 for technical details). Each regression and each average is carried out over all the CIMEL-lidar matched points for periods of interest (POIs) of the subclass D_{RS}. A "c" subscript is employed (rather than "D_{RS}") because of the limitations of the graphing program.